


Two-dimensional intrinsic ferrovalley Janus 2H-VSeS monolayer with high Curie temperature and robust valley polarization

Cunquan Li and Yukai An*

Key Laboratory of Display Materials and Photoelectric Devices, Ministry of Education, Tianjin Key Laboratory for Photoelectric Materials and Devices, National Demonstration Center for Experimental Function Materials Education, School of Material Science and Engineering, Tianjin University of Technology, Tianjin 300384, China

 (Received 18 July 2022; revised 11 September 2022; accepted 20 September 2022; published 29 September 2022)

Inspired by the unique physical properties of two-dimensional (2D) V-based Janus dichloride monolayers with intrinsic ferromagnetism and high Curie temperature T_c , we investigate the electronic structure, spin-valley polarization, and magnetic anisotropy of a Janus 2H-VSeS monolayer in detail using first-principles calculations. The results show that the Janus 2H-VSeS monolayer exhibits a large valley polarization of 105 meV, high T_c of 278 K, and in-plane magnetocrystalline anisotropy contributed by the $d_{x^2-y^2}/d_{xy}$ orbitals of V atoms. The biaxial strain ($-8\% < \varepsilon < 8\%$) can effectively tune the magnetic moments of the V atom, valley polarization ΔE , T_c , and magnetocrystalline anisotropy energy of the Janus 2H-VSeS monolayer. The corresponding ΔE and T_c are adjusted from 72 to 106.8 meV and from 180 to 340 K, respectively. Due to the broken space- and time-reversal symmetries, opposite valley charge carriers carry opposite Berry curvatures, which leads to prominent anomalous Hall conductivity at the K and K' valleys. The maximum modulation of Berry curvature can reach to 45% and 9.5% by applying the biaxial strain and charge carrier doping, respectively. The stable in-plane magnetocrystalline anisotropy and robust spontaneous valley polarization make the ferromagnetic Janus 2H-VSeS monolayer a promising material for achieving spintronic and valleytronic devices.

DOI: [10.1103/PhysRevMaterials.6.094012](https://doi.org/10.1103/PhysRevMaterials.6.094012)

I. INTRODUCTION

Since the successful discovery and synthesis of graphene [1], two-dimensional (2D) materials with hexagonal lattice structures have attracted a great deal of interest due to their excellent physical and chemical properties compared with their bulk counterparts [2]. As members of this 2D family, transition metal dichalcogenides (TMDs) MX_2 ($M = \text{Mo}, \text{W}$; $X = \text{S}, \text{Se}$) with a central M sublayer sandwiched by two mirror-symmetric X sublayers possess a tunable band gap (1–2 eV) and are good candidates for optoelectronic, valley electronic, and nanoelectronic devices [3,4]. Due to the lack of inversion symmetry, TMDs possess a pair of inequivalent degeneracy energy valleys at the K and K' points in momentum space and exhibit extraordinary quantum effects, such as valley-spin locking and valley-spin Hall effects [5–8]. The energy valley can be utilized and manipulated, making it an excellent information carrier for charge and spin to store information and perform logic operations. The biggest challenge in the development of valleytronics is to achieve the manipulation and generation of valley polarization by lifting the degeneracy between the K and K' valleys. To date, multiple pathways to lift the valley degeneracy have been studied, including circularly polarized light pumping [9], external magnetic fields [10], transition metal atom doping or adsorption [11], and the magnetic proximity effect [12]. However, the generated valley polarization will disappear and

return to the intrinsic paravalley states once the external field is removed, which is impracticable for application in valleytronic devices. Therefore, searching for 2D materials with intrinsic valley polarization is crucial. Generally, the long-range ferromagnetic ordering can be well preserved in 2D monolayers with intrinsic anisotropy caused by the spin-orbit coupling effect. This has been proved in the CrI_3 and VI_3 monolayer systems, which exhibit Curie temperatures T_c of 45 and 49 K, respectively [13–15]. Further, 2D ferrovalley monolayers (VS_2 [16], VSe_2 [17], and VTe_2 [18]) with intrinsic ferromagnetic ordering and spontaneous valley polarization have been successfully synthesized and have attracted considerable attention due to their strong magnetovalue coupling effects. The spontaneous valley polarization in V-based TMDs monolayers originates from the magnetic interaction between the V $3d$ electrons, which do not depend on the external fields and can achieve simultaneous manipulation of spin and valley degrees of freedom.

Stable Janus group VI chalcogenides MXY ($M = \text{Mo}, \text{W}$; $X, Y = \text{S}, \text{Se}, \text{Te}$; $X \neq Y$) were first proposed by Cheng *et al.* [19], and the Janus MoSSe was successfully synthesized via experiments using modified chemical vapor deposition (CVD) methods [20]. At the same time, some Janus systems, including Janus graphene [21], Janus graphene oxide [22], and group III chalcogenide $NN'X_2$ ($N, N' = \text{Ga}, \text{In}$; $N \neq N'$; $X = \text{S}, \text{Se}, \text{Te}$) [23] monolayers, have also been systematically investigated and exhibit extraordinary physical properties with a tunable electric dipole and high carrier mobility. Additionally, 2D Janus TMDs with intrinsic ferromagnetism, such as Janus MnXY ($X, Y = \text{S}, \text{Se}, \text{Te}$; $X \neq Y$) [24,25] and

*ayk_bj@126.com

$\text{Cr}(\text{I}, X)_3$ ($X = \text{Cl}, \text{I}, \text{and Br}$) [26] monolayers, have been proved to exhibit a large Dzyaloshinskii-Moriya interaction behavior [27]. The experimental realization of 2D ferrovalley materials, especially for the 2H-VSe₂ monolayer, may provide an exciting new platform for the Janus structure with intrinsic ferromagnetic semiconductors. Interestingly, the Janus 2H-VSeS monolayer was first predicted by Zhang *et al.* [28], and they comprehensively investigated its piezoelectricity, ferroelasticity, and valley polarization properties. It is expected that the ordered Janus 2H-VSeS monolayer can be grown using a modified CVD method similar to that described above and will introduce new physical phenomena. Therefore, it is significant to gain more insights into the intrinsic physical properties of the Janus 2H-VSeS monolayer.

In this work, the geometric structure, kinetic stability, Curie temperature T_c , magnetocrystalline anisotropy, and valley polarization of Janus 2H-VSeS monolayers under various biaxial strains and charge carrier doping are systematically discussed using first-principles calculations. The results show that the electronic structures of the Janus 2H-VSeS monolayer can be effectively modulated, which results in an obvious change in the magnetic moments of V atoms, valley polarization, band gap, and T_c . Furthermore, the Berry curvatures at the K and K' valleys show opposite signs due to the breaking of mirror symmetry along with the out-of-plane direction, which can also be effectively modulated by the biaxial strain and charge carrier doping. These results provide new insights for adjusting the electronic structure and magnetic properties of the Janus 2H-VSeS monolayer, which is very helpful for the design of new nanoelectronic devices.

II. COMPUTATIONAL METHODS

The first-principles calculations are performed using the plane-wave basis Vienna Ab initio Simulation Package (VASP) [29–32], based on the density functional theory (DFT). The generalized gradient approximation functional of Perdew, Burke, and Ernzerhof is adopted [33,34]. Considering the strongly correlated correction of V $3d$ localized electrons, the local spin-density approximation + U method is adopted [35], and the effective on-site Coulomb interaction parameter ($U = 2.00$ eV) and exchange interaction parameter ($J = 0.87$ eV) have been added to it [36,37]. A vacuum space of 18 Å in the z direction is set to avoid the adjacent interactions. The cutoff energy is set at 500 eV, and the criteria for energy and atom force convergence are 10^{-6} Å and 10^{-3} eV/Å⁻¹, respectively. The Brillouin zone is sampled with $16 \times 16 \times 1$ Γ -centered Monkhorst-Pack grids [38]. The effect of van der Waals corrections (DFT-D3 method) [39] is considered during the structure optimizations, and the VASPKIT [40] code is used to process the VASP data. The phonon spectrum and phonon density of states are calculated with PHONOPY [41] based on density-functional perturbation theory, and a $4 \times 4 \times 1$ supercell is used to calculate the Hessian matrix. The spin-orbit coupling (SOC) and noncollinear magnetism are considered in the calculations of electronic structure. For the calculation of Berry curvature and anomalous Hall conductivity, the maximally localized Wannier functions (MLWFs) are constructed using the WANNIER90 package [42,43]. In the case of the Janus 2H-VSeS monolayer, there are 22 bands in the energy range

from about -6 to 4 eV, mainly formed by V d orbitals and X ($X = \text{Se}, \text{S}$) p orbitals. Ten d orbitals on the V atom and six p orbitals on each X atom are chosen as the initial guess of the Wannier functions. After fewer than 400 iterative steps, the total Wannier spreads are well converged down to 10^{-6} Å². A fine k mesh of $30 \times 30 \times 1$ is used in the WANNIER interpolation. The Monte Carlo simulation procedure MCSOLVER [44,45] based on the Wolff algorithm of the classical Heisenberg model is used to estimate T_c . In the specified temperature interval, we completely thermalize the system to equilibrium with 120 000 scans starting from the ferromagnetic order, and all statistics are obtained from the next 720 000 scans.

III. RESULTS AND DISCUSSION

It has been reported that the trigonal prismatic (2H) phase is more energetically stable than the octahedral (1T) phase in the Janus VSeS monolayer [28]. Thus, the geometry of the Janus 2H-VSeS monolayer with a S-V-Se sandwich structure is fabricated with MEDEA-VASP materials design software, as shown in Fig. 1(a). After the optimization of the geometry, the corresponding V-Se and V-S bond lengths are 2.51 and 2.36 Å, respectively. The optimized lattice constant is 3.259 Å, which is between those of 2H-VS₂ (3.18 Å) and 2H-VSe₂ (3.34 Å) monolayers [17,46]. For the optimized geometry, the 2H-VSe₂ and 2H-VS₂ monolayers belong to the D_{3h} point group, while the Janus 2H-VSeS monolayer breaks the off-plane structure symmetry and presents the C_{3v} point group. The calculated average electrostatic potential along the z axis is rather asymmetric, as shown in Fig. 1(b). Obviously, the electrostatic potential of the S side is smaller than that of the Se side, namely, $V_S < V_{Se}$, implying a larger electronegativity of the S atom. Each V atom contributes a magnetic moment of $0.978\mu_B$ in the Janus 2H-VSeS monolayer. Meanwhile, the difference in electronegativity between the S and Se atoms can alter the local magnetic interaction, which induces a larger magnetic moment for the V atom. To confirm the magnetic ground states of the Janus 2H-VSeS monolayer, the ferromagnetic (FM) and antiferromagnetic (AFM) states in a $2 \times 2 \times 1$ supercell are calculated. The total magnetic moment is $4.0\mu_B$ for the Janus 2H-VSeS monolayer with a FM state, while the total magnetic moment is $0\mu_B$ with an AFM state. The ferromagnetic stability energy ($\Delta E = E_{\text{FM}} - E_{\text{AFM}}$) of the $2 \times 2 \times 1$ supercell is -260 meV < 0 , strongly suggesting that the Janus 2H-VSeS monolayer is an intrinsic ferromagnetic material. As is known, the Janus 2H-VSeS monolayer suffers from the spin wave, so the nonmagnetic ground state is a supercell with Peierls distortion, and the phonon dispersion is also considered to be unstable due to the presence of imaginary frequencies in the AFM state. Therefore, to estimate the stability of the Janus 2H-VSeS monolayer, the phonon spectrum and phonon density of states with the FM state are finally calculated in a $4 \times 4 \times 1$ supercell. As shown in Fig. 1(c), the absence of significant imaginary phonon modes over the whole Brillouin zone strongly suggests that the Janus 2H-VSeS monolayer is dynamically stable, which is consistent with the previous report [28]. The highest frequency is calculated to be 12.35 THz, which is between the reported values for the 2H-VSe₂ (10.02 THz) and 2H-VS₂ (13.7 THz) monolayers [46–48]. The contribution at low frequencies

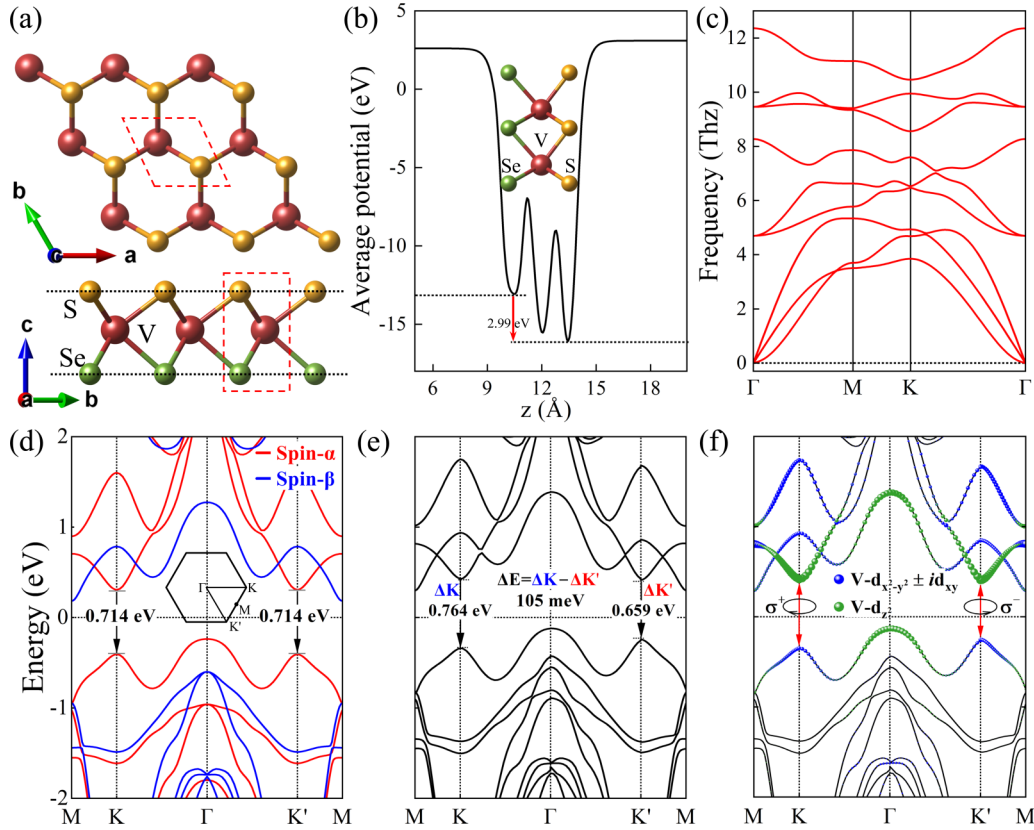


FIG. 1. (a) Top and side views of the Janus 2H-VSeS monolayer. The red, yellow, and green spheres represent V, S, and Se atoms, respectively. (b) The average electric potential along the z axis and (c) the phonon spectrum for the Janus 2H-VSeS monolayer. (d) The spin-polarized band structures of the Janus 2H-VSeS monolayer. The red and blue lines represent the spin-up (α) and spin-down (β) band structures. The inset is the first Brillouin zone containing the K and K' points. (e) The band structures of the Janus 2H-VSeS monolayer with SOC. (f) The V d orbital-resolved band structure of the Janus 2H-VSeS monolayer with SOC; the green and blue dots denote the contribution from the d_{z^2} and $d_{x^2-y^2}/d_{xy}$ orbitals of the V atom, respectively. The arrows between the VBM and the CBM denote the valley-selective optical transitions induced by left and right circularly polarized light σ^+ and σ^- .

($0 < \varepsilon < 5$ THz) mainly comes from the Se atoms, in contrast to the V and S atoms, which make the main contribution at high frequencies ($6 < \varepsilon < 12$ THz), as shown in Fig. S1 of the Supplemental Material (SM) [49]. It is maybe for that reason that the V (atomic weight: 50.94) and S (32.066) atoms are lighter than the Se (78.96) atoms. This can also remarkably affect the thermal properties of the Janus 2H-VSeS monolayer. At low temperature, the thermal conductivity is mainly contributed by the phonons of the low-frequency Se atom. However, at high temperature, the thermal conductivity is mainly contributed by phonons of higher-frequency V/S atoms. The spin-polarized band structure of the Janus 2H-VSeS monolayer is shown in Fig. 1(d). One can see that the valence band maximum (VBM) occupied by spin-up (α) electrons is located at the Γ point of the Brillouin zone, while the conduction band maximum (CBM) contributed by spin-down (β) electrons is located at the M point. Thus, the Janus 2H-VSeS monolayer is a bipolar magnetic semiconductor with an indirect energy gap of 0.407 eV. Clearly, there exists a Dirac valley contributed by the spin- α states at the K and K' points, as shown by the two black lines closest to the valley gap in Fig. 1(d). The two K and K' valleys are degenerate in energy with identical valley gaps of 0.714 eV. The band structures of the Janus 2H-VSeS monolayer with SOC are

shown in Fig. 1(e). It is obvious that the valley energies at the K and K' points in the conduction band remain close, while the energy at the K' point is higher than that at the K point in the valence band. Hence, the valley degeneracy is broken, inducing a large valley polarization ($\Delta E = \Delta K - \Delta K'$) of 105 meV, which is usually manifested as two split peaks in the photoluminescence spectrum. Figure 1(f) shows the V d orbital-resolved band structure of the Janus 2H-VSeS monolayer with SOC. Both the VBM and CBM at the K and K' points are mainly contributed by V atoms. At the two unequal K and K' valleys, the CBM is mainly contributed by the in-plane V $d_{x^2-y^2}/d_{xy}$ orbitals, while the VBM at the K and K' points is dominated by the V d_{z^2} orbital. Figure S2(a) of the SM [49] shows the corresponding three-dimensional band structure of the Janus 2H-VSeS monolayer with SOC. It is obvious that the energy of the VBM at the Γ point is the global maximum, while that at the K and K' points is only a local maximum. At the same time, the energy of the CBM at the K and K' points is also not globally minimal, and the global maximum is at the M point. The 2D projected band structure of the valence band and the conduction band at the $k_x k_y$ plane is shown in Figs. S2(b) and S2(c) of the SM [49]. Clearly, the six valleys within the Brillouin zone degenerate in energy with respect to each other. This indicates that the SOC

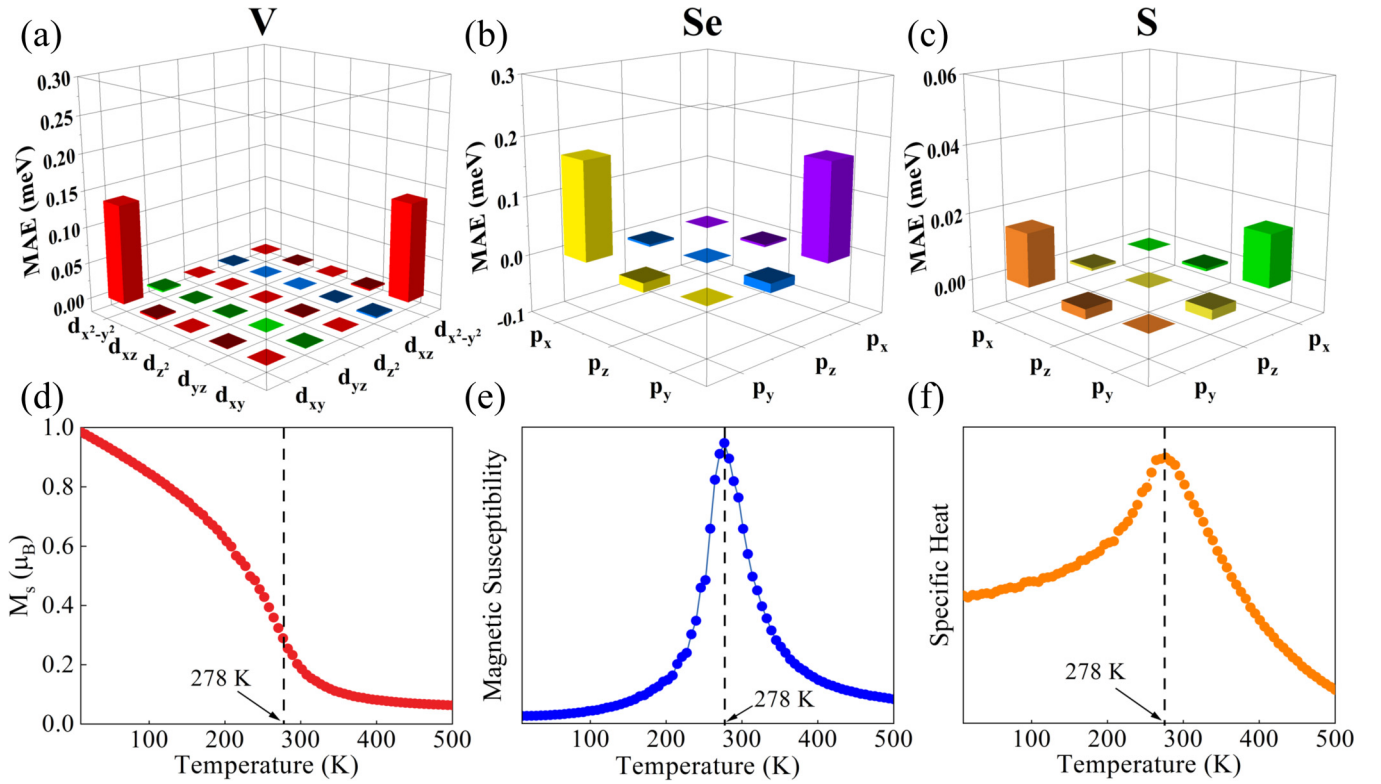


FIG. 2. (a)–(c) The V d and Se(S) p orbital-resolved MAEs of the Janus 2H-VSeS monolayer. Dependence of (d) the magnetic moment, (e) magnetic susceptibility, and (f) specific heat capacity on temperature for the Janus 2H-VSeS monolayer.

effect achieves large valley polarization in the Janus 2H-VSeS monolayer.

Considering the magnetic moment switching from the in-plane [100] axis to the out-of-plane [001] axis, the energy it spends is called magnetocrystal anisotropy energy (MAE). $\text{MAE}(E_{[001]} - E_{[100]})$ can be defined by the following equation:

$$\text{MAE} = \xi^2 \sum_{o,u} (|\langle o|L_x|u\rangle|^2 - |\langle o|L_z|u\rangle|^2) / (E_u - E_o), \quad (1)$$

where ξ , o , and μ are the SOC constants and E_o and E_u are the energies of the occupied and unoccupied states, respectively. $E_{[001]}$ and $E_{[100]}$ are the energies of the magnetization in the [001] and [100] directions, respectively. So a positive (negative) MAE value implies the in-plane (out-of-plane) easy axis. One can see from Eq. (1) that the orbital matrix element differences and energy differences together affect the MAE behavior, which can be used to analyze the contributions of different interorbit hybridizations to the MAE. The V d and Se(S) p orbital-resolved MAEs for the Janus 2H-VSeS monolayer are shown in Figs. 2(a)–2(c). The calculated total MAE value is 0.31 meV, and the corresponding MAE values contributed by the V d , Se p , and S p orbitals are 0.14, 0.15, and 0.01 meV, respectively. These strongly suggest that the Janus 2H-VSeS monolayer processes the in-plane magnetic anisotropy (IMA), which is mainly contributed by the hybridized V $d_{x^2-y^2}$ and d_{xy} orbitals as well as the Se(S) p_x and p_y orbitals.

T_c of ferromagnetic materials can be well calculated using the classical Heisenberg Monte Carlo model. In the

calculation, the spin Hamiltonian including the single-ion anisotropy can be described as follows:

$$H = -\frac{1}{2} \sum_{(i,j)} [J^x S_i^x S_j^x + J^y S_i^y S_j^y + J^z S_i^z S_j^z] - \sum_i D(S_i^z)^2. \quad (2)$$

For the entire V-atom lattice, (i, j) denotes the individual V atoms in the immediate vicinity, and i traverses the entire lattice. J and D are the spin-exchange parameter and magnetic anisotropy energy, respectively. $J > 0$ favors the ferromagnetic interactions, and $D > 0$ favors the out-of-plane easy axis. In the $4 \times 4 \times 1$ supercell, the energies of the FM and AFM states and the magnetic ion anisotropy parameter D with the SOC effect can be calculated as follows:

$$E_{\text{FM}} = E_0 - \left(\frac{1}{2} \times 6 \times 4\right) J |S|^2, \quad (3)$$

$$E_{\text{AFM}} = E_0 + 4 \times \left(-\frac{1}{2} \times 2 + \frac{1}{2} \times 4\right) J |S|^2, \quad (4)$$

$$J = \frac{E_{\text{AFM}} - E_{\text{FM}}}{16|S|^2}, \quad (5)$$

$$D = \frac{E_{\text{FM}}^\alpha - E_{\text{FM}}^z}{4S^2}, \quad (6)$$

where S ($S = 1/2$) is the spin operator and α and z are the directions along the in-plane [100] and the out-of-plane [001] axes, respectively. Usually, the subnearest neighbor V-V interactions are negligible in this system. Thus, only the nearest V-V interactions are considered in the calculation.

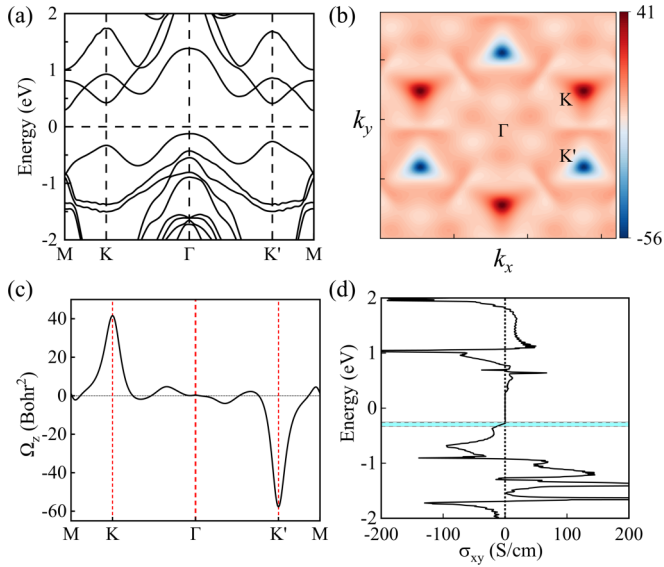


FIG. 3. (a) The band structure of the Janus 2H-VSeS monolayer calculated by MLWFs. Calculated Berry curvature of the Janus 2H-VSeS monolayer (b) over the 2D Brillouin zone and (c) along the high-symmetry lines. (d) Calculated anomalous Hall conductivity of the 2H-VSeS monolayer. The two parallel dashed lines indicate the two valley extremes.

The calculated exchanged parameter J and the magnetic ion anisotropy parameter D are 64 and -1.22 meV, respectively. Figures 2(d)–2(f) illustrate the dependence of the magnetic moment, magnetic susceptibility, and specific heat capacity on temperature for the Janus 2H-VSeS monolayer. The simulated T_c is as high as 278 K, which is close to room temperature (300 K).

In the case of inversion symmetry breaking in the Janus 2H-VSeS monolayer, the charge carriers also acquire a valley-contrast Berry curvature [50]. The z component of the Berry curvature $\Omega_n^z(k)$ of the occupied state band according to the Kubo formula [51,52] is calculated and can be expressed as

$$\Omega_n^z(k) = - \sum_{n \neq m} \frac{2 \operatorname{Im} \langle \Psi_{nk} | v_x | \Psi_{mk} \rangle \langle \Psi_{mk} | v_y | \Psi_{nk} \rangle}{(E_m - E_n)^2}, \quad (7)$$

where $|\Psi_{nk}\rangle$ is a calculated wave function of the Bloch states at k points with the energy eigenvalue E_n and $v_{x(y)}$ are velocity operators along the x and y directions, respectively. To ensure the accuracy of the Wannier basis functions, the tightly bound band structure is calculated using MLWFs, as shown in Fig. 3(a). The band structure is in good agreement with the DFT results [Fig. 1(e)], indicating that the resulting Wannier basis functions are sufficiently localized to ensure the precision and accuracy of the calculation. Figures 3(b) and 3(c) show the calculated results for Berry curvature over the Brillouin zone and along the high-symmetry line, respectively. In the intrinsic ferromagnetic field of the Janus 2H-VSeS monolayer, the Berry curvature has opposite signs at the K and K' points with different absolute magnitudes. Meanwhile, the integration of Berry curvature in the Brillouin zone gives the contribution to the anomalous Hall conductivity, which can be

expressed as

$$\sigma_{xy} = - \frac{e^2}{\hbar} \int_{\text{BZ}} \frac{d^2k}{(2\pi)^2} \Omega_n^z(k). \quad (8)$$

Due to the breaking of the time-reversal symmetry, a nonzero anomalous Hall conductivity calculated using WANNIERTOOLS [53] appears, as shown in Fig. 3(d). Since the Hall currents from the K and K' valleys do not disappear completely, a net charge current will be generated. Due to the presence of electric field E , the Berry curvature drives an anomalous transverse velocity [54]:

$$v = - \frac{e}{\hbar} E \times \Omega_n(k). \quad (9)$$

Since the CBM and VBM are mainly contributed by in-plane $d_{x^2-y^2}$ and d_{xy} orbitals for the Janus 2H-VSeS monolayer, it is predicted that the magnetic and electronic properties are strongly related to in-plane biaxial strain. To estimate the strain dependence of electronic properties, the in-plane biaxial strain is applied by the relation of $\varepsilon = [(a - a_0)/a_0] \times 100\%$, where a and a_0 present the lattice constants of strained and unstrained Janus 2H-VSeS monolayers. As shown in Fig. S3 of the SM [49], the total energies of FM and AFM states show monotonically asymptotic change with increasing the tensile strains ($\varepsilon = 2\%, 4\%, 6\%, 8\%$) and the compressive strains ($\varepsilon = -2\%, -4\%, -6\%, -8\%$). The ferromagnetic stability energy ΔE increases monotonically with increasing strain from -8% (165 meV) to 8% (318 meV). The distance between V atoms becomes smaller with continuously increasing compressive strain, which leads to an increase in superexchange interactions. However, the Janus 2H-VSeS monolayer consistently maintains the FM ground state under the various strains from -8% to 8% . The total MAE for the Janus 2H-VSeS monolayer under various strains is shown in Fig. 4(a). It is clear that the Janus 2H-VSeS monolayer still retains IMA character under various strains. The total MAE decreases linearly as the tensile strain increases from 0% to 8% . However, in the compressive strain range, the total MAE first increases and reaches a maximum value of 0.5 meV at a compressive strain of -6% , then gradually decreases from -6% to 0% . Figure 4(b) shows the V, Se, and S atomic-layer-resolved MAE under various strains. The MAEs from the S and V atoms decrease linearly as the strain increases from -8% to 8% , while that from the Se atom first increases to a maximum value at a strain of -6% and then gradually decreases, which is similar to the total MAE behavior. Interestingly, the V and Se/S atoms always maintain IMA character throughout the whole strain range. The main contribution of MAE to the Janus 2H-VSeS monolayer comes from the V and Se atoms, which is consistent with the fact that MAE can be contributed by nonmetallic atoms with stronger SOC [55]. Figures 4(c)–4(f) show the V d and Se p orbital-resolved MAEs for Janus 2H-VSeS monolayers under various strains, respectively. As the strain increases from -4% to 4% , the positive MAE of the Janus 2H-VSeS monolayer still mainly comes from the matrix element differences of the V atom ($d_{xy}/d_{x^2-y^2}$ orbitals) and of the Se atom (p_x/p_y orbitals). However, the matrix element difference of the Se (p_z/p_y orbitals) atom shows a transition from IMA to perpendicular magnetic anisotropy (PMA) character. The matrix

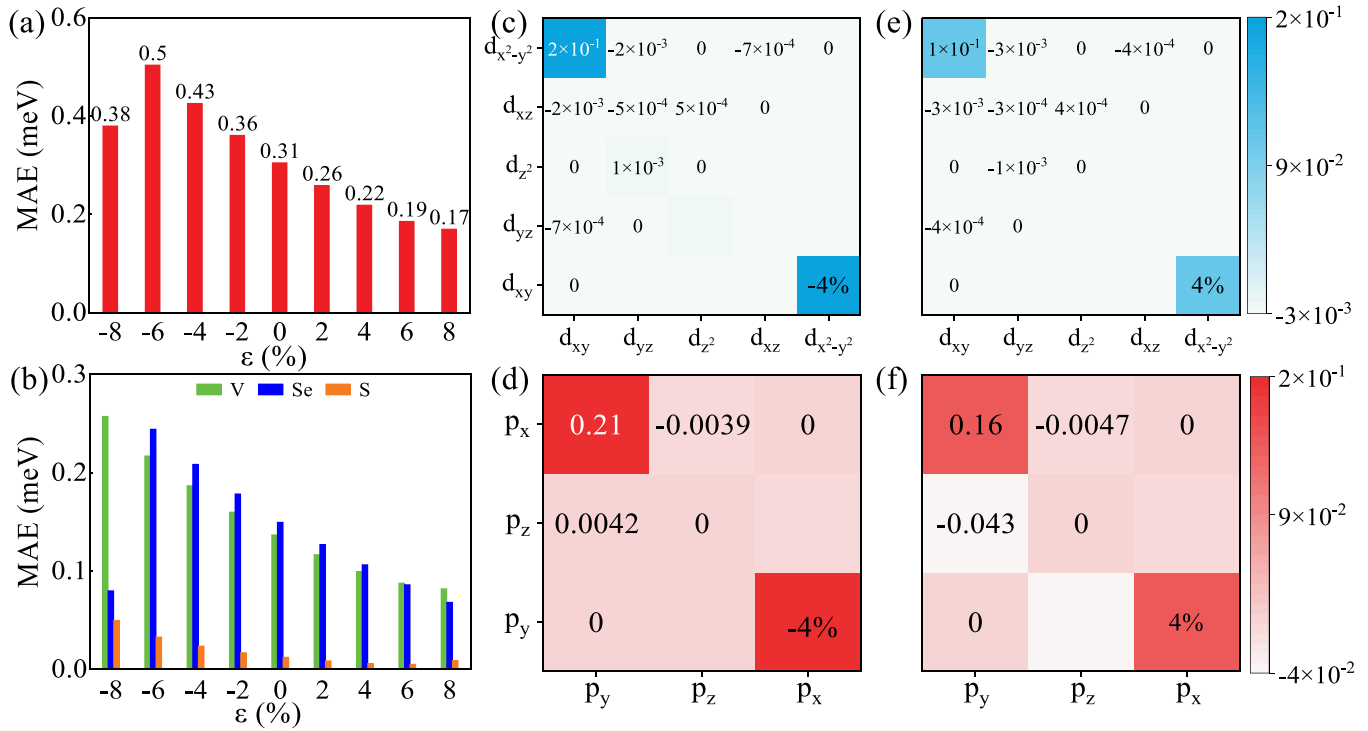


FIG. 4. (a) The total MAE for the Janus 2H-VSeS monolayer under various strains. (b) The V, Se, and S atomic-layer-resolved MAE for the Janus 2H-VSeS monolayer under various strains. The V *d* and Se *p* orbital-resolved MAE for the Janus 2H-VSeS monolayer at strains of (c) and (d) -4% and (e) and (f) 4% .

element difference of the S (p_x/p_y orbitals) atom still makes a rather small contribution to the MAE and is not shown in Fig. 4. Hence, the matrix element differences of the Se atom (p_x/p_y and p_z/p_y orbitals) and of the V atom ($d_{xy}/d_{x^2-y^2}$ orbitals) dominate the MAE behavior for the Janus 2H-VSeS monolayer under various biaxial strains.

Figure 5(a) shows the magnetic moment of the V atom and T_c for the Janus 2H-VSeS monolayer under various strains. At the tensile strain range ($\epsilon = 2\%, 4\%, 6\%$, and 8%), the corresponding magnetic moments of the V atom are $1.024\mu_B$, $1.052\mu_B$, $1.088\mu_B$, and $1.133\mu_B$, respectively. At the compressive strain range ($\epsilon = -2\%, -4\%, -6\%$, and -8%), the corresponding magnetic moments of the V atom are $0.968\mu_B$, $0.936\mu_B$, $0.899\mu_B$, and $0.861\mu_B$, respectively. It is obvious that the magnetic moment of the V atom shows a monotonic increase with increasing the strains from -8% to 8% . In fact, as the strain increases, the bond length between the V atoms increases, and the ionic-bond interaction overcomes the covalent-bond interaction. As a result, the number of unpaired electrons in the V atom increases, leading to an increase in the magnetic moment. This is consistent with the reported results in the 2H-VS₂ and 2H-VSe₂ monolayers [56]. One can see from Fig. 5(a) that as the strain increases from -8% to 8% , the corresponding T_c are 180 K (-8%), 189 K (-6%), 215 K (-4%), 247 K (-2%), 278 K (0%), 292 K (2%), 304 K (4%), 311 K (6%), and 340 K (8%), respectively, exhibiting a monotonic increase behavior. Apparently, this is due to the further enhancement of superexchange interaction with the increase of strain. The dependences of the magnetic moment of the V atom and specific heat capacity on the temperature under various strains are shown in Figs. 5(b) and 5(c), and the transition behavior is consistent with the above analysis.

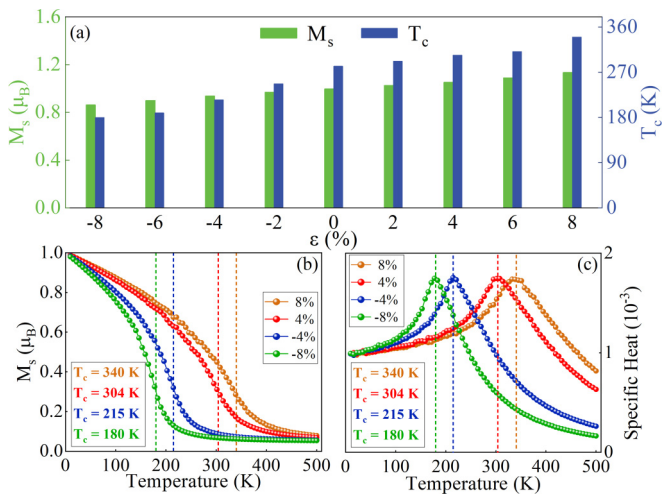


FIG. 5. (a) The magnetic moment of the V atom and T_c for the Janus 2H-VSeS monolayers under various strains. Dependence of (b) the magnetic moment and (c) specific heat capacity on the temperature for the Janus 2H-VSeS monolayer at strains of -8% , -4% , 4% , and 8% .

The band structures of Janus 2H-VSeS monolayers under various strains ($\pm 4\%$) with SOC are shown in Fig. 6(a). Clearly, strain can effectively adjust the band structures of the Janus 2H-VSeS monolayer accompanied by the bands up at the compressive strain (-4%) and the bands down at

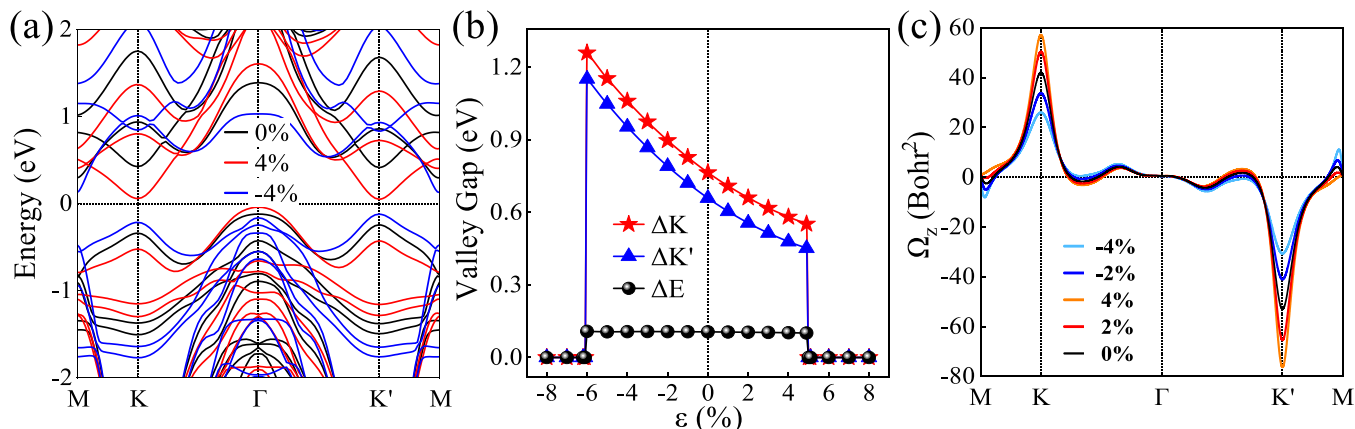


FIG. 6. (a) Band structures of Janus 2H-VSeS monolayers under various strains ($\pm 4\%$) with SOC. (b) Dependence of ΔK , $\Delta K'$, and valley polarization ΔE on the strain. (c) The Berry curvature of the Janus 2H-VSeS monolayers at strains of -4% , -2% , 0% , 2% , and 4% .

the tensile one (4%) with respect to the vacuum level [57]. Therefore, it is convinced that the valley degrees of freedom can be well tuned by applying the strain. Figure 6(b) shows the dependence of ΔK and $\Delta K'$ and valley polarization ΔE on the strain for the Janus 2H-VSeS monolayers. When the tensile strains ($\varepsilon = 1\%$, 2% , 3% , 4% , and 4.9%) are applied, the corresponding ΔK values are 709, 660, 618, 580, and 552 meV, while the $\Delta K'$ values are 604, 556, 514, 478, and 451 meV, respectively. For the compressive strains ($\varepsilon = -1\%$, -2% , -3% , -4% , -5% , and -6%), the corresponding ΔK values are 827, 897, 975, 1060, 1153, and 1260 meV, while the $\Delta K'$ values are 721, 790, 868, 953, 1048, and 1151 meV. Obviously, the ΔK and $\Delta K'$ values monotonously increase with increasing the strains from -6% to 4.9% . Surprisingly, ΔK and $\Delta K'$ values show a good quadratic dependence on the strain, namely, $\Delta K = 36\varepsilon^2 - 6.02\varepsilon + 0.7636$ and $\Delta K' = 37\varepsilon^2 - 5.96\varepsilon + 0.658$. The valley polarization ΔE first increases and reaches a maximum value of 106.8 meV at a strain of -4% and then gradually decreases with further increasing the strain from -3% to 5% . Therefore, the valley polarization of the Janus 2H-VSeS monolayer can be well modulated by the strain. The Berry curvature of Janus 2H-VSeS monolayers at strains of -4% , -2% , 0% , 2% , and 4% is shown in Fig. 6(c). At $\varepsilon = 4\%$, the maximum modulation of Berry curvature can reach 45%. The tensile (compressive) strain tends to increase (decrease) the Berry curvature as well as their magnitude difference $|\Omega_n^z(K) + \Omega_n^z(K')|$. Since the anomalous Hall conductivity is defined as the integral sum of Berry curvature in the Brillouin zone and the Berry curvature is nonzero only around the K and K' points, the anomalous Hall conductivity is expected to be greatly enhanced under tensile strains. In this way, one can adjust the transverse Hall voltage by applying strain. As is well known, charge carrier doping can be considered an effective method to modulate the electronic structure and Fermi level of semiconductors. It has been reported that the electrical, magnetic, and valley properties of 2H-VS₂ [58], 2H-VSe₂ [17], and 2H-WSe₂ [59] monolayers can be well tuned by charge carrier doping, which can also be expected for the Janus 2H-VSeS monolayer due to the presence of unpaired electrons in the V $3d$ orbitals. The MAE and exchange energy J for the Janus 2H-VSeS monolayer with various charge carrier dopings are shown

in Figs. 7(a) and 7(b). It is obvious that the MAE shows a gradual decrease trend with increasing the hole or electron doping concentration. Interestingly, the electron doping does not alter the IMA character of Janus 2H-VSeS monolayer. On the contrary, the IMA character is transformed into the PMA character when the hole doping concentration is above $-0.3e$. On the other hand, the exchange energy J still remains a positive value under various electron (hole) doping concentrations ($0-0.5e$), strongly suggesting that the transition from the FM to AFM states does not occur. J first increases to a maximum value of 69.2 meV at a hole doping concentration of $-0.1e$ and then gradually decreases with increasing the carrier doping concentration from $-0.1e$ to $0.5e$. Compared to the undoped case, the maximum modulation of MAE and J values can reach 82% (218%) and 98% (65%) by electron (hole) doping, respectively. The band structures of the Janus

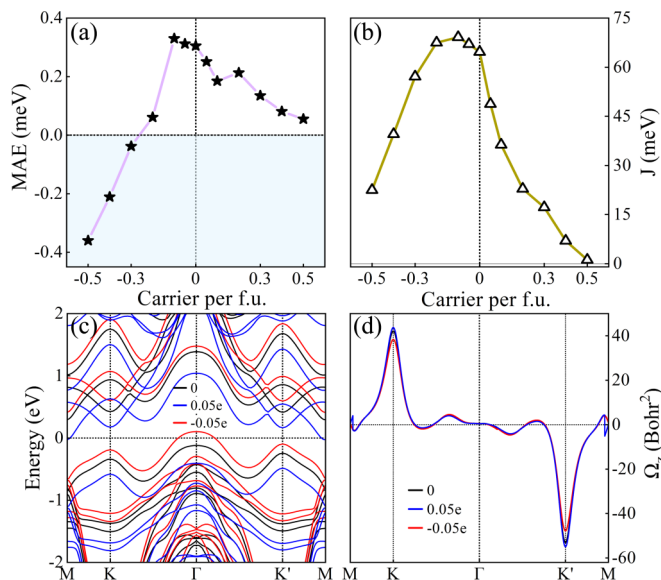


FIG. 7. (a) The MAE and (b) exchange energy J for the Janus 2H-VSeS monolayer with various charge carrier dopings. (c) The band structures and (d) Berry curvature for the Janus 2H-VSeS monolayer with 0.05 hole and 0.05 electron doping, respectively. The Fermi level is set to zero.

2H-VSeS monolayer with hole (electron) doping is shown in Fig. 7(c). It is clear that the Fermi level shifts to the VBM (CBM) with the introduction of a hole (electron) concentration of $0.05e$, implying that the charge carrier doping can effectively modulate the band structures and position of the Fermi level. The lack of time-reversal symmetry and mirror symmetry makes the electronic structure of the Janus 2H-VSeS monolayer more tunable compared with nonmagnetic TMDs. The control of valley freedom by charge carrier doping is also investigated and shown in Fig. 7(d). Obviously, for the Janus 2H-VSeS monolayer doped with holes (electrons), the peak intensity of the Berry curvature $\Omega_n^z(k)$ at the K and K' points become weaker (stronger). The modulation of $\Omega_n^z(k)$ can reach 3.8% (9.5%) by doping with an electron (hole) concentration of $0.05e$. It is obvious that compared to the biaxial strain modulation, the charge carrier doping has a smaller effect on $\Omega_n^z(k)$. As shown in Fig. S4 of the SM [49], a valleytronic device for the Janus 2H-VSeS monolayer can be constructed based on the calculated results of the Berry curvature $\Omega_n^z(k)$ and the anomalous Hall conductivity. With charge carrier doping, the Fermi level of the Janus 2H-VSeS monolayer can be modulated between the K valley (ΔK) and the K' valley ($\Delta K'$). As an example of proper hole doping, when an in-plane electric field E is applied, the Janus 2H-VSeS monolayer is magnetized upwards, and spin holes from the K' valley flow upwards. The accumulated holes generate a charge Hall current that can be measured as a positive voltage. On the contrary, when reversing the Janus 2H-VSeS monolayer or modulating magnetized downwards, the spin holes accumulated while flowing to the lower K valley can be measured as a negative voltage. This device can be used as a spin filter, filtering out all carriers with spin up and spin down to move laterally, which will produce a net Hall current. In summary, the Janus 2H-VSeS monolayer can be applied to

anomalous Hall effect valley electronics devices and become the basis for valley electronics applications.

IV. CONCLUSIONS

In summary, the geometry, magnetic, electronic, and valley properties of the Janus 2H-VSeS monolayer were investigated in detail using first-principles calculations. The Janus 2H-VSeS monolayer exhibits an indirect band-gap semiconductor character with a ferromagnetic Curie temperature T_c of 278 K, in-plane MA, and a large spontaneous valley polarization of 105 meV. Interestingly, as the strain increases from -8% to 8% , the magnetic moment of the V atom and T_c show a monotonous increase trend, while the valley polarization and MAE first increase and gradually decrease. By analyzing the $3d$ orbital-resolved MAE of V atoms based on second-order perturbation theory, the contributions to the MAE mainly originate from the matrix element differences between the d_{xy} and $d_{x^2-y^2}$ orbitals of V atoms. The strong SOC effect, Berry curvature, and anomalous Hall conductivity under broken inversion symmetry can also be efficiently tuned by applying strain (modulation range: 45%) and charge carrier doping (modulation range: 9.5%), indicating that the valley polarization of the Janus 2H-VSeS monolayer is robust against the external biaxial strains and charge carrier doping. Finally, a valley and spin filter device was designed based on the calculation results. The versatility of the Janus 2H-VSeS monolayer with considerable MAE, high T_c , and large valley polarization strongly suggests its potential application in two-dimensional spintronic devices.

ACKNOWLEDGMENT

This work was supported by the Natural Science Foundation of Tianjin City (Grant No. 20JCYBJC16540).

-
- [1] K. S. Novoselov, A. K. Geim, S. V. Morozov, D. Jiang, M. I. Katsnelson, I. Grigorieva, S. Dubonos, and A. Firsov, *Nature (London)* **438**, 197 (2005).
 - [2] K. He, B. Barut, S. Yin, M. D. Randle, R. Dixit, N. Arabchigavkani, J. Nathawat, A. Mahmood, W. Echtenkamp, and C. Binek, *Adv. Mater.* **34**, 2105023 (2022).
 - [3] A. M. Afzal, M. Z. Iqbal, G. Dastgeer, A. U. Ahmad, and B. Park, *Adv. Sci.* **8**, 2003713 (2021).
 - [4] S. Xu, C. Si, Y. Li, B.-L. Gu, and W. Duan, *Nano Lett.* **21**, 1785 (2021).
 - [5] R. Ahammed and A. De Sarkar, *Phys. Rev. B* **105**, 045426 (2022).
 - [6] Q. Cui, Y. Zhu, J. Liang, P. Cui, and H. Yang, *Phys. Rev. B* **103**, 085421 (2021).
 - [7] Y. Ominato, J. Fujimoto, and M. Matsuo, *Phys. Rev. Lett.* **124**, 166803 (2020).
 - [8] M. Yagmurcukardes, Y. Qin, S. Ozen, M. Sayyad, F. M. Peeters, S. Tongay, and H. Sahin, *Appl. Phys. Rev.* **7**, 011311 (2020).
 - [9] K. F. Mak, K. He, J. Shan, and T. F. Heinz, *Nat. Nanotechnol.* **7**, 494 (2012).
 - [10] Y. Zhang, K. Shinokita, K. Watanabe, T. Taniguchi, Y. Miyauchi, and K. Matsuda, *Adv. Funct. Mater.* **31**, 2006064 (2021).
 - [11] G. Aivazian, Z. Gong, A. M. Jones, R.-L. Chu, J. Yan, D. G. Mandrus, C. Zhang, D. Cobden, W. Yao, and X. Xu, *Nat. Phys.* **11**, 148 (2015).
 - [12] X. Liang, L. Deng, F. Huang, T. Tang, C. Wang, Y. Zhu, J. Qin, Y. Zhang, B. Peng, and L. Bi, *Nanoscale* **9**, 9502 (2017).
 - [13] T. Kong, K. Stolze, E. I. Timmons, J. Tao, D. Ni, S. Guo, Z. Yang, R. Prozorov, and R. J. Cava, *Adv. Mater.* **31**, 1808074 (2019).
 - [14] M. Baskurt, I. Eren, M. Yagmurcukardes, and H. Sahin, *Appl. Surf. Sci.* **508**, 144937 (2020).
 - [15] B. Huang, G. Clark, E. Navarro-Moratalla, D. R. Klein, R. Cheng, K. L. Seyler, D. Zhong, E. Schmidgall, M. A. McGuire, and D. H. Cobden, *Nature (London)* **546**, 270 (2017).
 - [16] C. Shen, G. Wang, T. Wang, C. Xia, and J. Li, *Appl. Phys. Lett.* **117**, 042406 (2020).
 - [17] J. Liu, W.-J. Hou, C. Cheng, H.-X. Fu, J.-T. Sun, and S. Meng, *J. Phys.: Condens. Matter* **29**, 255501 (2017).
 - [18] C. Wang and Y. An, *Appl. Surf. Sci.* **538**, 148098 (2021).

- [19] Y. Cheng, Z. Zhu, M. Tahir, and U. Schwingenschlöggl, *Europhys. Lett.* **102**, 57001 (2013).
- [20] A.-Y. Lu, H. Zhu, J. Xiao, C.-P. Chuu, Y. Han, M.-H. Chiu, C.-C. Cheng, C.-W. Yang, K.-H. Wei, and Y. Yang, *Nat. Nanotechnol.* **12**, 744 (2017).
- [21] F. Li and Y. Li, *J. Mater. Chem. C* **3**, 3416 (2015).
- [22] A. C. de Leon, B. J. Rodier, Q. Luo, C. M. Hemmingsen, P. Wei, K. Abbasi, R. Advincula, and E. B. Pentzer, *ACS Nano* **11**, 7485 (2017).
- [23] Y. Guo, S. Zhou, Y. Bai, and J. Zhao, *Appl. Phys. Lett.* **110**, 163102 (2017).
- [24] J. Liang, W. Wang, H. Du, A. Hallal, K. Garcia, M. Chshiev, A. Fert, and H. Yang, *Phys. Rev. B* **101**, 184401 (2020).
- [25] J. Yuan, Y. Yang, Y. Cai, Y. Wu, Y. Chen, X. Yan, and L. Shen, *Phys. Rev. B* **101**, 094420 (2020).
- [26] C. Xu, J. Feng, S. Prokhorenko, Y. Nahas, H. Xiang, and L. Bellaiche, *Phys. Rev. B* **101**, 060404(R) (2020).
- [27] I. Dzyaloshinsky, *J. Phys. Chem. Solids* **4**, 241 (1958).
- [28] C. Zhang, Y. Nie, S. Sanvito, and A. Du, *Nano Lett.* **19**, 1366 (2019).
- [29] G. Kresse and J. Furthmüller, *Comput. Mater. Sci.* **6**, 15 (1996).
- [30] G. Kresse, J. Furthmüller, and J. Hafner, *Phys. Rev. B* **50**, 13181 (1994).
- [31] G. Kresse and J. Furthmüller, *Phys. Rev. B* **54**, 11169 (1996).
- [32] G. Kresse and D. Joubert, *Phys. Rev. B* **59**, 1758 (1999).
- [33] J. P. Perdew, K. Burke, and M. Ernzerhof, *Phys. Rev. Lett.* **77**, 3865 (1996).
- [34] P. Söderlind, O. Eriksson, B. Johansson, and J. M. Wills, *Phys. Rev. B* **50**, 7291 (1994).
- [35] P. Hohenberg and W. Kohn, *Phys. Rev.* **136**, B864 (1964).
- [36] S. Grimme, *J. Comput. Chem.* **25**, 1463 (2004).
- [37] A. I. Liechtenstein, V. I. Anisimov, and J. Zaanen, *Phys. Rev. B* **52**, R5467 (1995).
- [38] H. J. Monkhorst and J. D. Pack, *Phys. Rev. B* **13**, 5188 (1976).
- [39] S. Grimme, J. Antony, S. Ehrlich, and H. Krieg, *J. Chem. Phys.* **132**, 154104 (2010).
- [40] V. Wang, N. Xu, J.-C. Liu, G. Tang, and W.-T. Geng, *Comput. Phys. Commun.* **267**, 108033 (2021).
- [41] A. Togo and I. Tanaka, *Scr. Mater.* **108**, 1 (2015).
- [42] N. Marzari, A. A. Mostofi, J. R. Yates, I. Souza, and D. Vanderbilt, *Rev. Mod. Phys.* **84**, 1419 (2012).
- [43] A. A. Mostofi, J. R. Yates, Y.-S. Lee, I. Souza, D. Vanderbilt, and N. Marzari, *Comput. Phys. Commun.* **178**, 685 (2008).
- [44] L. Liu, X. Ren, J. Xie, B. Cheng, W. Liu, T. An, H. Qin, and J. Hu, *Appl. Surf. Sci.* **480**, 300 (2019).
- [45] L. Liu, S. Chen, Z. Lin, and X. Zhang, *J. Phys. Chem. Lett.* **11**, 7893 (2020).
- [46] H. L. Zhuang and R. G. Hennig, *Phys. Rev. B* **93**, 054429 (2016).
- [47] M. Esters, R. G. Hennig, and D. C. Johnson, *Phys. Rev. B* **96**, 235147 (2017).
- [48] H. Zhang, L.-M. Liu, and W.-M. Lau, *J. Mater. Chem. A* **1**, 10821 (2013).
- [49] See Supplemental Material at <http://link.aps.org/supplemental/10.1103/PhysRevMaterials.6.094012> for more simulation results on the phonon DOS, three-dimensional band structure, energies of FM/AFM configurations, and a valleytronic device of the Janus 2H-VSeS monolayer.
- [50] D. Xiao, W. Yao, and Q. Niu, *Phys. Rev. Lett.* **99**, 236809 (2007).
- [51] D. J. Thouless, M. Kohmoto, M. P. Nightingale, and M. den Nijs, *Phys. Rev. Lett.* **49**, 405 (1982).
- [52] Y. Yao, L. Kleinman, A. H. MacDonald, J. Sinova, T. Jungwirth, D.-S. Wang, E. Wang, and Q. Niu, *Phys. Rev. Lett.* **92**, 037204 (2004).
- [53] Q. Wu, S. Zhang, H.-F. Song, M. Troyer, and A. A. Soluyanov, *Comput. Phys. Commun.* **224**, 405 (2018).
- [54] D. Xiao, M.-C. Chang, and Q. Niu, *Rev. Mod. Phys.* **82**, 1959 (2010).
- [55] B. Yang, X. Zhang, H. Yang, X. Han, and Y. Yan, *J. Phys. Chem. C* **123**, 691 (2019).
- [56] Y. Ma, Y. Dai, M. Guo, C. Niu, Y. Zhu, and B. Huang, *ACS Nano* **6**, 1695 (2012).
- [57] D. Zhang and S. Dong, *Prog. Nat. Sci.* **29**, 277 (2019).
- [58] N. Luo, C. Si, and W. Duan, *Phys. Rev. B* **95**, 205432 (2017).
- [59] R. Mukherjee, H. J. Chuang, M. R. Koehler, N. Combs, A. Patchen, Z. X. Zhou, and D. Mandrus, *Phys. Rev. Appl.* **7**, 034011 (2017).